Computers and Geotechnics 137 (2021) 104250

Contents lists available at ScienceDirect

Computers and Geotechnics

journal homepage: www.elsevier.com/locate/compgeo

Discrete element modelling of the 4-sided impact roller

Yue Chen *, Mark B. Jaksa, Yien-Lik. Kuo, Brendan T. Scott

School of Civil, Environmental and Mining Engineering, University of Adelaide, SA 5005, Australia

ARTICLE INFO

Keywords:
Rolling dynamic compaction
Impact roller
Compaction
Ground improvement
Discrete element method

ABSTRACT

Rolling dynamic compaction (RDC) is a ground improvement technique, which involves towing a non-circular module behind a tractor to achieve soil compaction. When compared against conventional static and vibratory compaction techniques, RDC is capable of compacting thicker layers of soil and at a faster operating speed. This study validates the developed numerical scale model against a field study using the full-size RDC module. Numerical results were compared with the field data in four aspects namely, displacements at the ground surface, and at depths of 0.7 and 1.1 m, pressures at 0.7 and 1.1 m depths, energy delivered by the RDC module into the underlying soil, and the depth of improvement. It is concluded that, numerical results are in good agreement with the field data. This paper also proposes that pressure results are an imperfect indicator to assess the optimum number of RDC passes, whereas, ground settlement is recommended since it better reflects ground improvement due to RDC and it has a clear relationship with the number of passes.

1. Introduction

It goes without saying that, for those who knew Prof. Scott Sloan, appreciated his great fondness for and his significant expertise in numerical modelling. This paper is offered humbly in honour of that great man, who continues to be deeply missed.

Soil compaction is a process where air voids within the soil body are removed and the density of the soil is increased by the application of mechanical energy. As a result, ground performance is improved with, for example, increased bearing capacity, enhanced strength, and reduced settlements and permeability (Ranjan and Rao, 2007). Rolling dynamic compaction (RDC) is a ground improvement technique which has gained increased popularity over the past few decades. It involves towing a non-circular module, which imparts energy as it falls to impact the ground. Both potential and kinetic energies are imparted into the ground simultaneously by RDC which, when compared with conventional smooth drum rollers, enables the ground to be compacted to a greater depth and with improved efficiency due to its relatively fast operating speed. RDC has been applied in several large and open ground improvement projects in the civil and mining sectors, land reclamation projects, and highway rehabilitation (Avalle and Carter, 2005; Avalle and McKenzie, 2005; Bouazza and Avalle, 2006).

Previous researchers have conducted field tests to assess the effectiveness of RDC (Avalle and Carter, 2005; Jaksa et al., 2012; Scott and Jaksa, 2014; Scott et al., 2019a, 2019b, 2020). As conducting field tests with the full-size RDC module is somewhat costly and time-consuming, and results obtained from such field testing contain some uncertainties due to the difficulty of controlling and measuring many aspects affecting the efficacy of RDC in the field. As a consequence, a 1:13 small-scale physical RDC model was investigated to assess the effectiveness of RDC in a controlled laboratory environment. Chung et al. (2017) confirmed that the small-scale model produced similar compaction results to those from the full-size model, based on the scaling laws proposed by Altaee and Fellenius (1994). Although conducting small-scale model tests is more cost effective than undertaking field tests, small-scale tests still require significant time, care and specialised equipment to prepare and undertake such testing. Therefore, numerical models have been developed by several researchers (Kuo et al., 2013; Bradley et al., 2019) to assess the effectiveness of RDC. Kuo et al. (2013) and Bradley et al. (2019) investigated the behaviour of a full-size RDC model using the finite element method (FEM) as incorporated in the LS-DYNA computer application (LSTC, 2018). The FEM model was validated against field results and it showed encouraging results in terms of simulating ground responses induced by RDC. However, one of the main disadvantages of the FEM model, due to its continuum rather than particulate nature, is that the motion of soil particles is difficult to simulate. To overcome the limitations of the FEM, the discrete element method (DEM) has been adopted by several researchers to simulate the

* Corresponding author.
E-mail addresses: yue.chen@adelaide.edu.au (Y. Chen), mark.jaksa@adelaide.edu.au (M.B. Jaksa), yien.kuo@adelaide.edu.au (Y.-Lik. Kuo), brendan.scott@adelaide.edu.au (B.T. Scott).

https://doi.org/10.1016/j.compgeo.2021.104250

Available online 8 June 2021

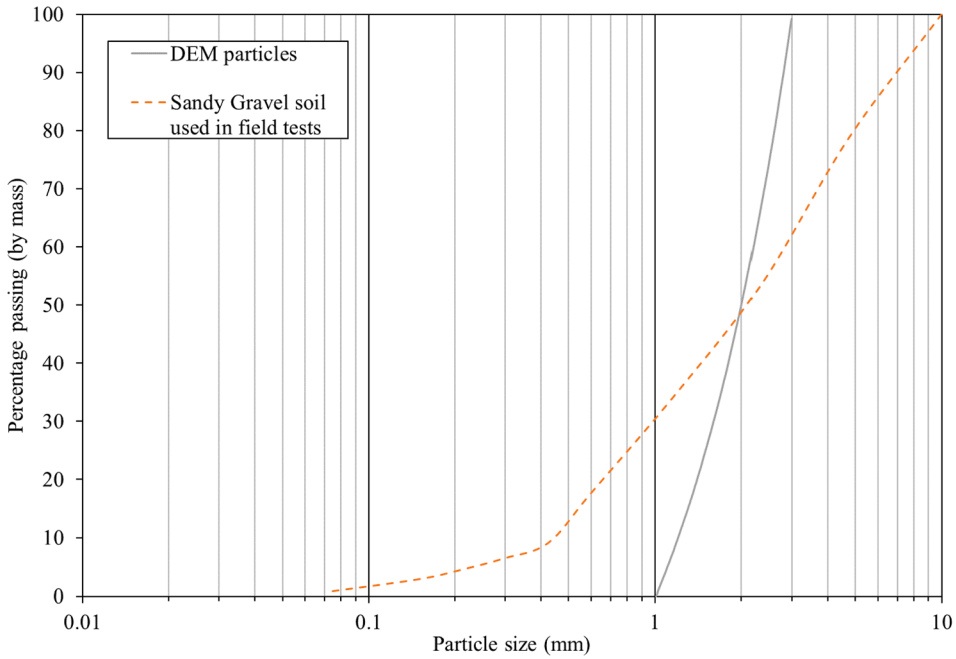

Fig. 1. Particle size distribution curves.

behaviour of granular materials (Jiang et al., 2014; Chen et al., 2018; Jing et al., 2018). In the DEM, particle displacements are tracked at each time step, which provides detailed information of soil movements at the particle scale. Since the FEM has been successfully used to model the behaviour of RDC (Kuo et al., 2013; Bradley et al., 2019), but it is unable to simulate non-continuum mechanics within a soil body influenced by RDC, and the DEM is able to model particle movements and interactions, but it is difficult to simulate the behaviour of RDC. The FEM-DEM approach is used to simulate soil responses due to RDC in order to combine the advantages of these two methods. The RDC module is described by the FEM and the soil particles are simulated by the DEM. The FEM-DEM approach has been successfully adopted to assess the wear of a tipper using LS-DYNA (Forsström and Jonsén, 2016) and to simulate tire-soil interactions (Yang et al., 2019; Xu et al., 2020; Zeng et al., 2020). These studies demonstrate the efficacy of the combined FEM-DEM approach in investigating problems related to geomechanics.

Air voids within the soil are reduced with each pass of the roller and therefore the performance of RDC is affected by the number of passes. As a result, settlement, shear strength and density of the soil increase with each pass of the RDC module, however, the rate of increase of these gradually diminishes with respect to the number of passes. Ultimately, when the number of passes reaches some critical value, settlement, shear strength and density will plateau. This is supported by Avalle and Grounds (2004) who identified a reducing rate of settlement change with increasing number of passes. The number of passes required is dependent on the type of soil, its initial density, and the characteristics of the RDC module; i.e. its mass, shape and operating speed. The changes in the rate of ground improvement indicate the optimum number of passes needs to be determined to achieve the desired densification of soils without conducting excessive number of passes. However, the optimum number of passes varies depending on the soil type, moisture content, gradation, and layer thickness of the soil (Avsar et al., 2006). In addition, the optimum number of passes is often quantified using different indicators in field conditions. For example, Avsar et al. (2006) defined the optimum number of passes by measuring the dry density of soil, whereas Avalle and McKenzie (2005) determined the optimum

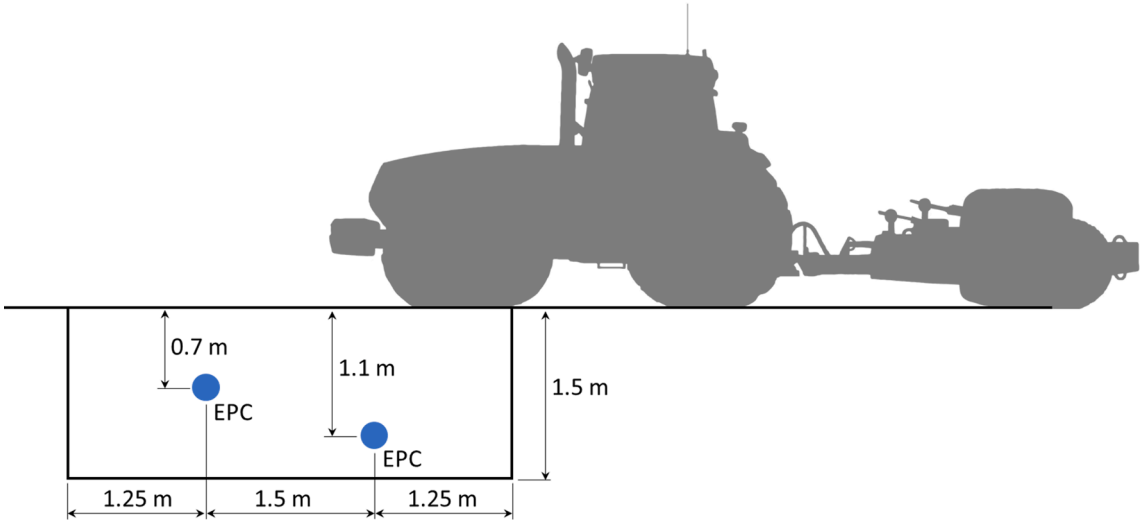

Fig. 2. Setup of the field tests.

number of passes by monitoring the average ground settlements, and Avalle and Carter (2005) used settlement, and the results of dynamic cone penetrometer (DCP) testing and cone penetrometer tests (CPTs). Some indicators can be measured in a cost-effective way; for example, ground settlement, and some are more time-consuming and costly; such as, DCP testing and CPTs. In order to determine the optimum number of passes, and in consideration of time, cost and feasibility, it is essential to obtain an indicator, which is not only easier to be measured, but also reflects the ground improvement induced by RDC. In current practice, the specified number of roller passes is often determined by the project engineer, since the optimum number of passes depends on the site conditions. Therefore, there is a need to obtain an efficient indicator that can be measured easily to determine the optimum number of passes of RDC under various field conditions.

This paper aims, firstly, to develop a FEM-DEM based model to simulate the behaviour of the 1:13 RDC scale model of the 4-sided, 8-tonne, Broons BH-1300 impact roller. Results of the developed numerical model are subsequently upscaled, using the Altaee and Fellenius (1994) scaling laws, and then validated against a field study that was conducted using the corresponding full-size RDC. Secondly, the results of the numerical model are analysed, evaluated, and compared against each other in order to obtain an efficient indicator that can be used to quantify the optimum number of RDC passes.

2. Field testing

A field study was carried out by Scott et al. (2016) and Scott et al. (2019a; 2019b; 2020) using the full-size 4-sided, 8-tonne, Broons BH-1300 impact roller at Monarto Quarries, Callington, South Australia. The field test was conducted on a trial pad which was filled with improved crushed rock quarry material, that was classified as a well-graded Sandy Gravel (GW) in accordance with the Unified Soil Classification System. The field particle size distribution curve is shown in Fig. 1. As shown in Fig. 2, the trial pad was 1.5 m deep and 4 m length, and two Geokon 3500 (230 mm diameter and 6 mm thick) earth pressure cells (EPCs) were placed at 0.7 and 1.1 m depths beneath the ground surface to measure pressures induced by RDC, respectively. Both EPCs were embedded at the centreline of the test lane. In addition, an accelerometer was attached to each EPC at Z plane to measure vertical acceleration. Both EPCs and accelerometers were connected to a custom-built data acquisition system and Labview software program. A sampling frequency of 4 kHz was used to ensure true peak pressures and accelerations could be captured. Acceleration-time responses were double integrated to quantify displacements at depths of 0.7 and 1.1 m beneath the ground surface. In addition, ground surface settlements were monitored by surveying local low points from each module face that contacted the ground. A total of 80 passes was conducted in the field trial, whilst maintaining a constant operating speed of 11 km/h.

One limitation of conducting field tests using buried EPCs is that it is not possible to capture the maximum pressure that the module imparts to the ground for every pass. To account for this, the distance between the centre of the module face and the centre of each EPC, defined as the offset distance, was measured to account for the effects of non-direct impacts.

3. Numerical model development

The FEM-DEM numerical model is developed using LS-DYNA to analyse the behaviour of an impact roller model on granular materials. The 1:13 scaled RDC module, rather than the full-size module, is simulated in this study due to computational and time constraints. The full-size module requires larger soil areas to be compacted that requires a greater number of soil particles in the numerical model. This will then significantly increase the simulation running time. In the numerical model, the actual soil particles are simulated using rigid spheres with deformable contacts. The rotation of spheres is prohibited to increase the macroscopic shear strength of the numerical model (Calvetti et al., 2003). The linear contact model developed by Cundall and Strack (1979) is adopted to describe the forces between particles. As shown in Fig. 3, the interaction between two overlapping particles is represented by two linear elastic springs in the normal and shear directions with constant stiffnesses of k_n and k_s, respectively; two viscous damping dashpots in the normal and shear directions with damping ratios of β_n and β_s, respectively; and a frictional slip in the shear direction with a coefficient of friction, μ, to limit the shear force between particles at contacts, based on Coulomb's law of friction. The interaction distance (d_{int}) between adjacent particles is defined by Eq. (1). The contact law is active when d_{int} is less than zero. Small numerical normal and shear damping ratios (i.e. $\beta_n = \beta_s = 0.1$) are selected for the soil particles in all of the simulations, considering the value of the restitution coefficient and the simulation of the triggering of failure (Gabrieli et al., 2009).

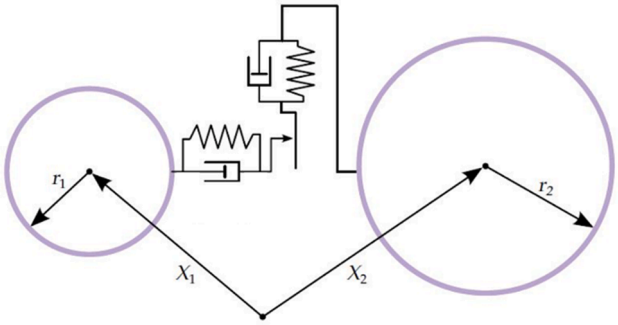

Fig. 3. Illustration of particle–particle contact interaction (LSTC, 2018).

$$d_{int} = r_1 + r_2 - |X_1 - X_2| \tag{1}$$

where r_1 and r_2 are the radii of two particles; and X_1 and X_2 are the coordinates of two particles.

Similar to the interaction between the particles, the interaction between finite elements and discrete particles is accommodated by a penalty-based contact algorithm, which checks each particle for penetration through the contact surface of the finite elements (LSTC, 2018). If penetration is detected, the contact force is applied between the penetrating particle and the contact point of the finite elements. The magnitude of the contact force is proportional to the penetration depth. This is treated by inserting springs between the discrete particles and the contact finite elements. The stiffnesses of these springs are calculated using Eq. (2). In the case of contact between elements with different stiffnesses, LS-DYNA adopts the lowest stiffness. If there is slide between the discrete particles and the contact finite elements, a friction force is also applied.

$$k_i = \frac{f_s \cdot A_i \cdot K_i}{V_i} \tag{2}$$

where k_i is the stiffness of the spring (i) placed between particles and the contact finite elements;f_s is the penalty scale factor (the default value of unity is used in this study); andA_i, V_i and K_i are the contact area, the volume and the stiffness of the contacted element, respectively.

Different from the FEM model, where the macroscopic properties of soil can be used as input parameters directly, in the DEM model, the input parameters need to be calibrated so that the numerical particles have the same macroscopic behaviour as the actual soil. Therefore, standard geotechnical tests, such as, direct shear or triaxial tests, are often undertaken to calibrate the DEM input parameters (Coetzee, 2017). In this study, the DEM input parameters are calibrated against triaxial tests and then the calibrated DEM input parameters are adopted in the numerical RDC simulations. All simulations were conducted on a supercomputer (2 × Intel Xeon Gold 6248 Processor @2.4 GHz) using the ANSYS (LS-DYNA) software.

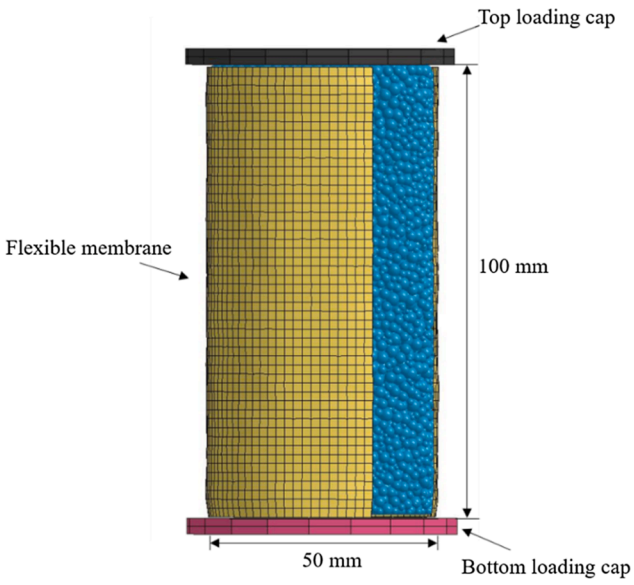

Fig. 4. Numerical triaxial tests.

3.1. Establishment of DEM input parameters

The laboratory triaxial tests under the confining pressures of 150 and 250 kPa were undertaken on Sandy Gravel soil from Monarto Quarries (as used in the field tests). The tests were drained and, hence, with no porewater pressure generated during the tests. As shown in Fig. 1, the soil particle size range was approximately 0.1–10 mm, with a D_{50} value of 2 mm. In the DEM model, particles were generated by specifying minimum and maximum radii. Because of time and computational constraints, it was impossible to use the same particle sizes in the numerical simulations as those adopted in experimental tests. The selection of the maximum and minimum DEM particle sizes is limited by the total number of particles, the time step for the numerical model, the diameter of the triaxial test samples, and the dimensions of the 1:13 RDC scale model. Small particle sizes significantly increase the total number of DEM particles and decrease the numerical time step, which then increases the simulation running time. The maximum particle size is governed by the diameter of the triaxial test samples in the calibration tests and the dimensions of the RDC scale model in the numerical RDC tests (this is treated in greater detail in the following section). In addition, a wide range of particle sizes results in a greater number of particles in the model, which increases the difficulty of particle size upscaling and significantly increases the simulation running time. As a consequence, a relatively narrow range of particle size is favoured (de Bono et al., 2015; Chen et al., 2018). Therefore, the minimum and maximum radii of the numerical particles are selected to be 0.5 and 1.5 mm, respectively, which yielded a $D_{50} = 2$ mm. The value of D_{50} is chosen to represent the Sandy Gravel soil used in the field tests. The particle size distribution curve of DEM particles is shown in Fig. 1.

As shown in Fig. 4, the numerical triaxial test model consists of two loading caps, a flexible membrane and soil particles. The numerical triaxial test sample has a diameter of 50 mm and a height of 100 mm, which are the same as those adopted in the laboratory triaxial tests. The loading caps and the flexible membrane are simulated using the FEM as rigid and rubber materials, respectively. The input parameters for the loading caps are referred to Zeng et al. (2020) and are presented in Table 1. The material properties of the membrane are defined by inputting the stress–strain curve obtained from uniaxial tension experiments reported by Thakur and Penumadu (2020) into the numerical model. The friction coefficient between the particles and the membrane, and between the particles and the loading caps are obtained from a numerical inclined plane test that has been employed by several researchers (Chou et al., 2012; González-Montellano et al., 2012; Coetzee, 2016), which are 0.67 and 0.7, respectively. The bottom loading cap is fixed and the top loading cap displaces in the vertical direction.

Similar to the laboratory triaxial tests, the numerical triaxial tests are simulated in three stages. Firstly, the DEM particles are generated randomly to fill an enclosed cylinder and then fall into the membrane under gravity. The top loading cap slightly moves up and down to compact the particles to match the laboratory porosity value. In the second stage, the confining pressures (150 and 250 kPa) are applied to the loading caps and the membrane simultaneously in all directions and are maintained during the tests. In the third stage, the top loading cap displaces vertically at a constant rate to shear the sample. A series of different loading rates are tested and a loading rate of 10 mm/s is used in all of the triaxial test simulations to optimise computational time and simulation accuracy while ensures the model is in a quasi-static condition during the shearing stage.

By trial-and-error, the numerical and laboratory results are shown in Fig. 5. It can be seen that, the numerical model provides similar stress–strain curves to those obtained experimentally, at both 150 and 250 kPa confining pressures. Prior to reaching the peak, the numerical results are slightly higher than those obtained experimentally at both confining pressures. For a confining pressure of 150 kPa, the peak strength predicted by the numerical model is slightly lower than that measured in the laboratory. Some differences between the numerical and laboratory volumetric responses are observed in Fig. 5b, which may be explained by the adoption of spherical particles in the numerical model (Zhou et al., 2021). In general, however, the numerical results are in very good agreement with the laboratory results. Table 1 summarises the calibrated DEM input parameters.

3.2. Numerical RDC simulations

The calibrated DEM input parameters are adopted in the numerical RDC simulations. As shown in Fig. 6, the numerical RDC model consists of a simplified 1:13 scale model of the roller, a chamber filled with soil particles and two timber frames. The chamber and timber frames are simulated using the FEM as rigid bodies and fixed at their initial locations, with no movement or deformation permitted during the compaction process. The size of the chamber is selected as 600 × 280 × 125 mm (length × width × height), considering the width of the module and the total number of particles in the numerical model. The height of the chamber has been demonstrated to be sufficient for compaction simulations, since the displacements of the soil particles located near the bottom of the chamber are negligible after 25 module passes, and it was reported by Chen et al. (2021), that the most significant compactive effects occur within the upper 100 mm depth. In addition, non-reflecting boundary conditions are applied to the DEM particles located near the boundaries of the chamber to prevent stress wave reflections. Since soil displacements are constrained by the edges of the chamber, ground improvement occurred in the middle region of the chamber is analysed extensively to quantify the effectiveness of RDC. The roller module with dimensions of 115 × 115 × 100 mm (height × length × width) is modelled using finite elements and defined to be a rigid body with a Young's modulus of elasticity of 210 GPa and Poisson's ratio of 0.28. As stated by Kuo et al. (2013) and Bradley et al. (2019), the roller deformation during compaction is negligible, since the roller is effectively rigid relative to the stiffness of the underlying soil. The friction coefficient between the particles and the roller module is 0.57, which is again obtained from the numerical inclined plane test. The motion (both horizontal and rotational speeds) of the roller module is defined in the numerical RDC model according to the operating speed of the full-size module in the field trial. The vertical speed is not constrained in the simulations, i.e. the numerical model predicts the module behaviour with respect to soil deformation. The initial starting position of the module for each pass was varied to simulate the same phenomenon that

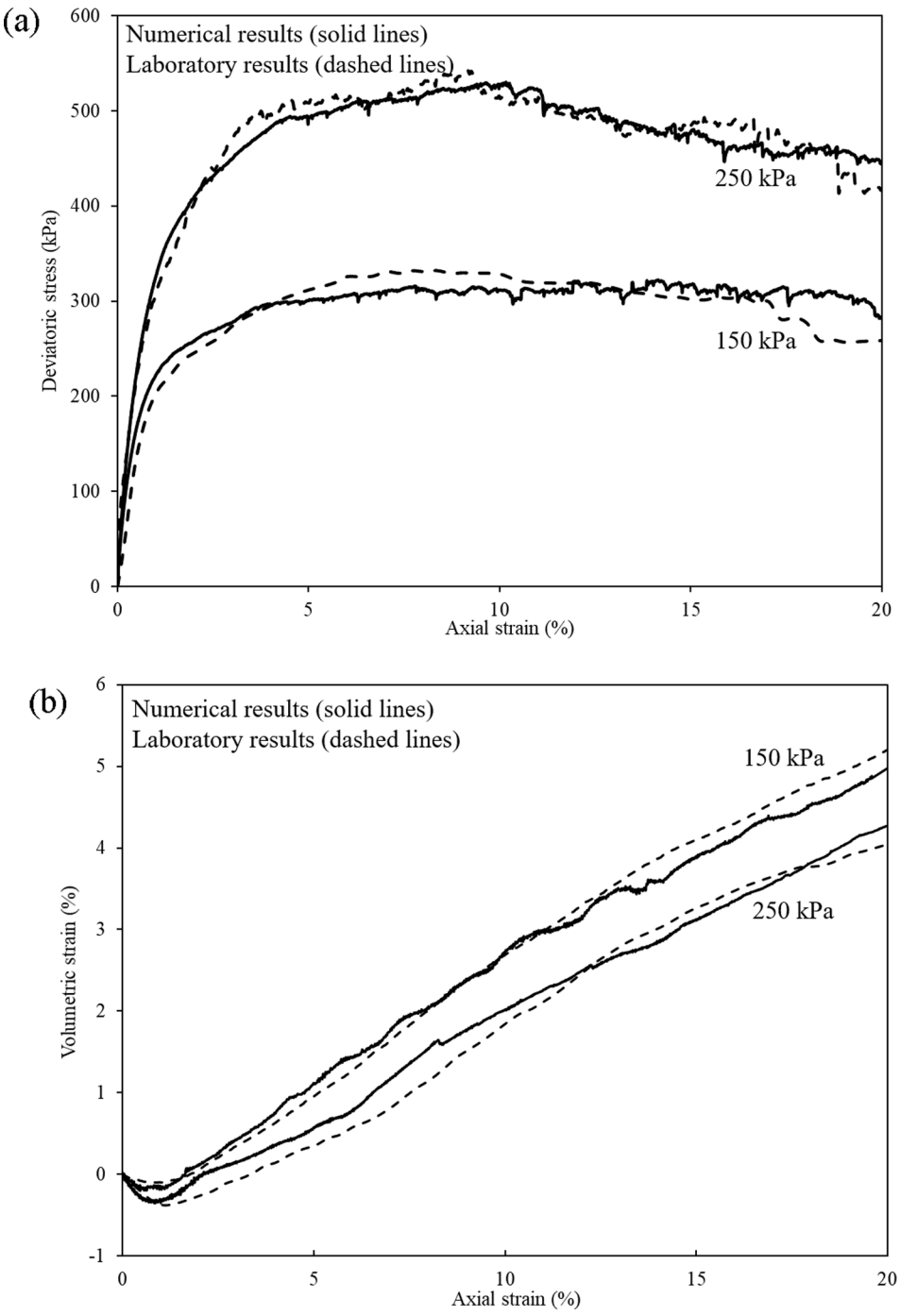

Fig. 5. Experimental and numerical triaxial test results at confining pressures of 150 and 250 kPa: (a) stress–strain curves, (b) volumetric curves.

Table 1
Calibrated DEM input parameters.

Parameter	Value
Particle density (kg/m^3)	2,620
Particle diameter (mm)	1–3
Coefficient of friction	0.25
Normal and shear stiffnesses (k_n and k_s) (N/m)	6.5×10^5
Normal and shear damping ratios (β_n and β_s)	0.1
Young's modulus of loading caps (MPa)	7,200
Poisson's ratio of loading caps	0.25

occurs in field operation.

In the numerical RDC simulations, the DEM particles are generated in a similar manner to that adopted in the numerical triaxial tests. Particles are generated randomly to fill a rectangular box and fall into the chamber under gravity. Subsequently, a rigid plate is placed on the top of DEM particles and it is moved up and down to compact the particles slightly to assist the particles to settle in the chamber. After the particle assembly reaches a static and steady state, the rigid plate is removed and the RDC process commences. Because of limitations associated with computational resources, the scaling approach proposed by Evans and Valdes (2011) is adopted to upscale the particle size distribution curve used in the calibration tests to reduce the total number of particles in the model and the simulation time. This scaling approach has

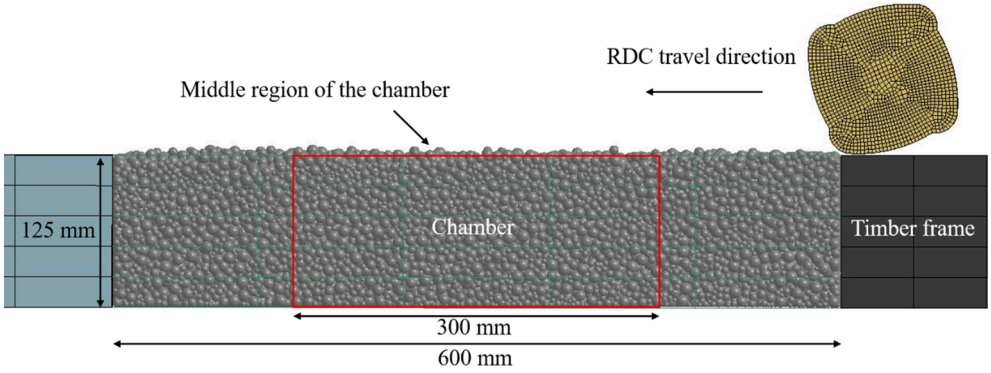

Fig. 6. Setup of numerical RDC simulations.

Table 2
Scaled DEM input parameters.

Parameter	Value
Particle density (kg/m^3)	2,620
Particle diameter (mm)	3.5–10.5
Coefficient of friction	0.25
Normal and shear stiffnesses (k_n and k_s) (N/m)	2.275×10^6
Normal and shear damping ratios (β_n and β_s)	0.1

been adopted in several DEM studies (e.g. Ciantia et al., 2015; Ciantia et al., 2016; Chen et al., 2018; Zhang et al., 2019) and has been demonstrated to be useful in replicating the behaviour of particle assemblies. The upper limit of particle scaling is governed by the relevant dimensions of the model (Ciantia et al., 2015). It is stated that the D_{50} of the scaled particles should be at least one order of magnitude lower than the relevant dimensions of the model. In addition, soil with maximum particle sizes of approximately 10 mm was adopted in the physical 1:13 RDC scale model tests performed by Chung et al. (2017) and no particle size effects were observed. Therefore, all DEM particles are upscaled uniformly to 3.5–10.5 mm, which then yields approximately 54,000 particles in the simulations (the soil initial void ratio in the numerical RDC simulations is 0.76). As mentioned above, to avoid size effects, the D_{50} of the scaled particles (7 mm) is one order of magnitude lower than the width of the roller module (100 mm). In order to preserve the macroscopic response of the particle assembly after scaling, the calibrated DEM input parameters are scaled accordingly, to account for the particle scaling factor (Feng and Owen, 2014; Ciantia et al., 2015), which is 3.5 in this study. Table 2 displays the upscaled DEM input parameters.

The stability of the numerical model is related to the adopted time step. The equations of motion in LS-DYNA are solved based on the explicit central difference scheme. Since both the FEM and DEM are used in this study, the critical time step (Δt) is calculated using the Eqs. (3)–(6) (Nakashima and Oida, 2004; Lei and Zang, 2010; LSTC, 2018). In this study, the time step is controlled by Δt_{DEM}, which is 2.87×10^{-6} s.

$$\Delta t \leq min\{\Delta t_{DEM}, \Delta t_{FEM}\} \tag{3}$$

$$\Delta t_{DEM} = TSSFAC \cdot 0.2 \cdot \pi \cdot \sqrt{\frac{m}{k_n}} \tag{4}$$

$$\Delta t_{FEM} = \frac{l_{min}}{c} \tag{5}$$

$$c = \sqrt{\frac{E(1-\nu)}{(1+\nu)(1-2\nu)\rho}} \tag{6}$$

where Δt_{DEM} and Δt_{FEM} are the critical time steps for the discrete and finite elements, respectively; *TSSFAC* is a time step scale factor in LS-DYNA, and the default value of $TSSFAC = 0.9$ is used in this simulation; m and k_n are the mass and normal stiffness of the DEM particles, respectively; l_{min} is the minimum effective length of the finite elements; c is the velocity of the elastic wave; and E, ν and ρ are the Young's modulus, Poisson's ratio and the mass density of the finite elements, respectively.

3.3. Scaling laws

In order to compare the scale model results against those of the full-size RDC, the standard scaling laws for scale model testing under a normal (1g) gravity condition developed by Altaee and Fellenius (1994) were adopted. These scaling laws have been successfully used to upscale the results of the physical 1:13 RDC scale model tests conducted by Chung et al. (2017). The scaling laws are not only used to scale properties of the scale module itself, e.g. converting properties of the full-size model to the scaled module [Eqs. (7)–(9)], but are also used to upscale the results obtained from the scale model [Eqs. (10)–(12)]. Under 1-g conditions, the soil shows different behaviour since it is subjected to different stress conditions in the full-scale and the small-scale models. As proposed by Altaee and Fellenius (1994), the constitutive similarity is preserved in the small-scale model, if the initial soil states in the full-scale and the small-scale models have equal proximity to the steady state line. The steady state of soil is selected as the reference state since soil at the steady state is independent of the initial state. Since Chung et al. (2017) employed the same soil as the present study and found that the slope of the steady state line, $\lambda = 0.11$, that value has been adopted here. The geometric scale ratio, n, is 1/13 in this study.

$$\frac{L_m}{L_p} = n \tag{7}$$

$$\frac{M_m}{M_p} = n^3 \tag{8}$$

$$\frac{V_m}{V_p} = n \tag{9}$$

$$\frac{D_m}{D_p} = n \cdot \frac{\frac{\Delta e_m}{1+e_{0m}}}{\frac{\Delta e_p}{1+e_{0p}}} \tag{10}$$

$$\frac{\sigma_m}{\sigma_p} = \exp\left(\frac{e_{0p} - e_{0m}}{\lambda}\right) \tag{11}$$

$$\frac{E_m}{E_p} = \exp\left(\frac{e_{0p} - e_{0m}}{\lambda}\right) \times n^3 \tag{12}$$

where L is the characteristic length; M is the mass of the roller module; V represents the operating speed; D is soil vertical displacement; σ is the imposed stress in the soil; E is the energy imparted by the roller mod-

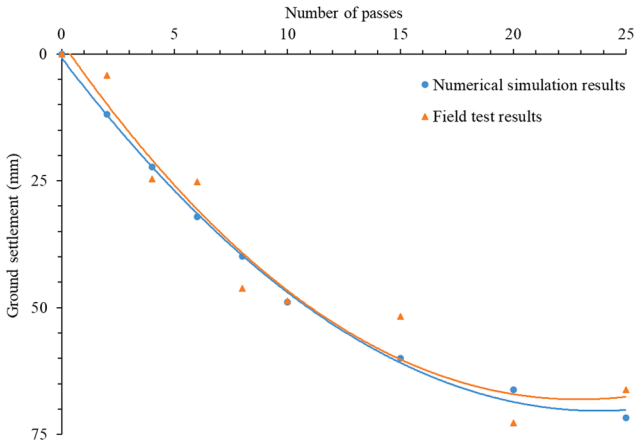

Fig. 7. Ground settlements obtained from the numerical model and field tests with respect to number of passes.

ule;n is the geometric scale ratio; e_0 is the initial void ratio; Δe is the change in void ratio; λ is the slope of the steady state line in the $e - \log \sigma$ plane; and the subscripts m and p denote the scale model and prototype (full-size module in this context), respectively.

Therefore, based on Eqs. (7)–(9), the numerical 1:13 RDC scale model simulations are conducted with a 3.64 kg module operated at a speed of 235 mm/s, which corresponds to the 8-tonne prototype module travelling at 11 km/h, as adopted in the field tests. Pressures and accelerations were measured at 0.7 and 1.1 m depths below the ground in the field trial. Therefore, measurements are taken at 55 and 85 mm depths beneath the ground in the numerical simulations. In field trial, soil initial void ratio varied with depth due to the complex natural of the soil. The average initial void ratio and the initial void ratio of the soil near 0.7 and 1.1 m depths were approximately 0.52, 0.507 and 0.5, respectively (Scott et al., 2016). The average void ratio after 25 module passes in the numerical tests is approximately 0.66. The average void ratio after 25 module passes in the field tests was approximately 0.46, which is inferred from the change in ground settlement with respect to the number of passes, since the void ratio was measured only before and after 80 module passes in the field tests. These void ratios are substituted into Eqs. (10)–(12) to obtain the scaling factor for each parameter. Due to time and computational constraints, the numerical RDC simulations consist of 25 module passes. As a point of reference, one RDC simulation, consisting of 25 passes and approximately 54,000 particles, typically took approximately 30 days to run at 12 CPU cores using the supercomputer mentioned above. It is worth mentioning that, the number of employed CPU cores is constrained by the number of available ANSYS licenses.

4. Comparisons between numerical model and field trial

Numerical results are compared with those from the field trials by examining four different parameters namely, displacements at the ground surface, and at depths of 0.7 and 1.1 m, pressures at 0.7 and 1.1 m depths, energy delivered by the RDC module into the underlying soil, and the depth of major improvement. These are each presented in turn.

4.1. Soil vertical displacements

Soil displacement is an important indicator of the soil behaviour as a consequence of RDC. Soil displacements at different depths within the numerical simulations are calculated by averaging all particle displacements at the depth of interest within the middle region of the chamber as shown in Fig. 6. These are presented in Figs. 7–9 and are upscaled using Eq. (10) based on average void ratios of the soil measured before and after compaction in the field study (0.52 and 0.46, respectively) and in the numerical model (0.76 and 0.66, respectively). Ground settlements obtained from the numerical model, together with field tests, are displayed in Fig. 7. As can be seen from both the numerical simulations and the field tests, the ground settlement increases with the number of passes. Two trend lines are used to fit the numerical and field results, and the shape of the two trend lines is very similar. It can be observed that the numerical model predicts the field test results very well. The numerical model predicts the ground settlement of 71.7 mm after 25 module passes, which is very close to that measured in field tests of 66.2 mm, with a difference of 5.5 mm (8.3%). This discrepancy can be explained by the limitations of the less accurate surveying method used in the field and the simplification of adopting spherical DEM particles in the numerical model. In summary, the results show that the numerical model is able to predict, reasonably well, soil settlements induced by RDC.

Vertical displacements obtained from the numerical model and field tests at 0.7 and 1.1 m depths are presented in Fig. 8. It is important to note that field displacements were calculated by integrating vertical accelerations, measured by accelerometers, with respect to time. As shown in Fig. 2, the length of field test pad was 4 m, and each accelerometer was placed 1.25 m from the edge of the test pad. As a result, field displacements are obtained from one location along the entire length of the test pad and, as such, do not represent average soil displacements at the test depths of 0.7 and 1.1 m. Therefore, the field displacements are presented in Fig. 8 for reference purposes. This also highlights a significant limitation with field testing, which is the difficulty of obtaining high fidelity measurements of internal soil displacements. In contrast, the numerical model provides great flexibility in this regard as it enables the movement of every individual particle to be tracked. In general, the soil displacements increase with increasing compactive effort. When compared against the field results, the numerical model yields much smoother vertical displacement results since the numerical displacements at 0.7 and 1.1 m depths are calculated by averaging the displacements of all of the soil particles at each depth (approximately 500 particles) within the central region of the chamber.

The numerical vertical displacements with depth, as presented in Figs. 7 and 8, are combined and superimposed in Fig. 9. As can be seen, each of the three curves show a trend of increasing vertical displacement with number of passes, but tends to plateau after approximately 20 passes. In addition, it can be observed that, as expected, the soil displacements decrease with increasing depth due to the dissipation of compactive energy with depth.

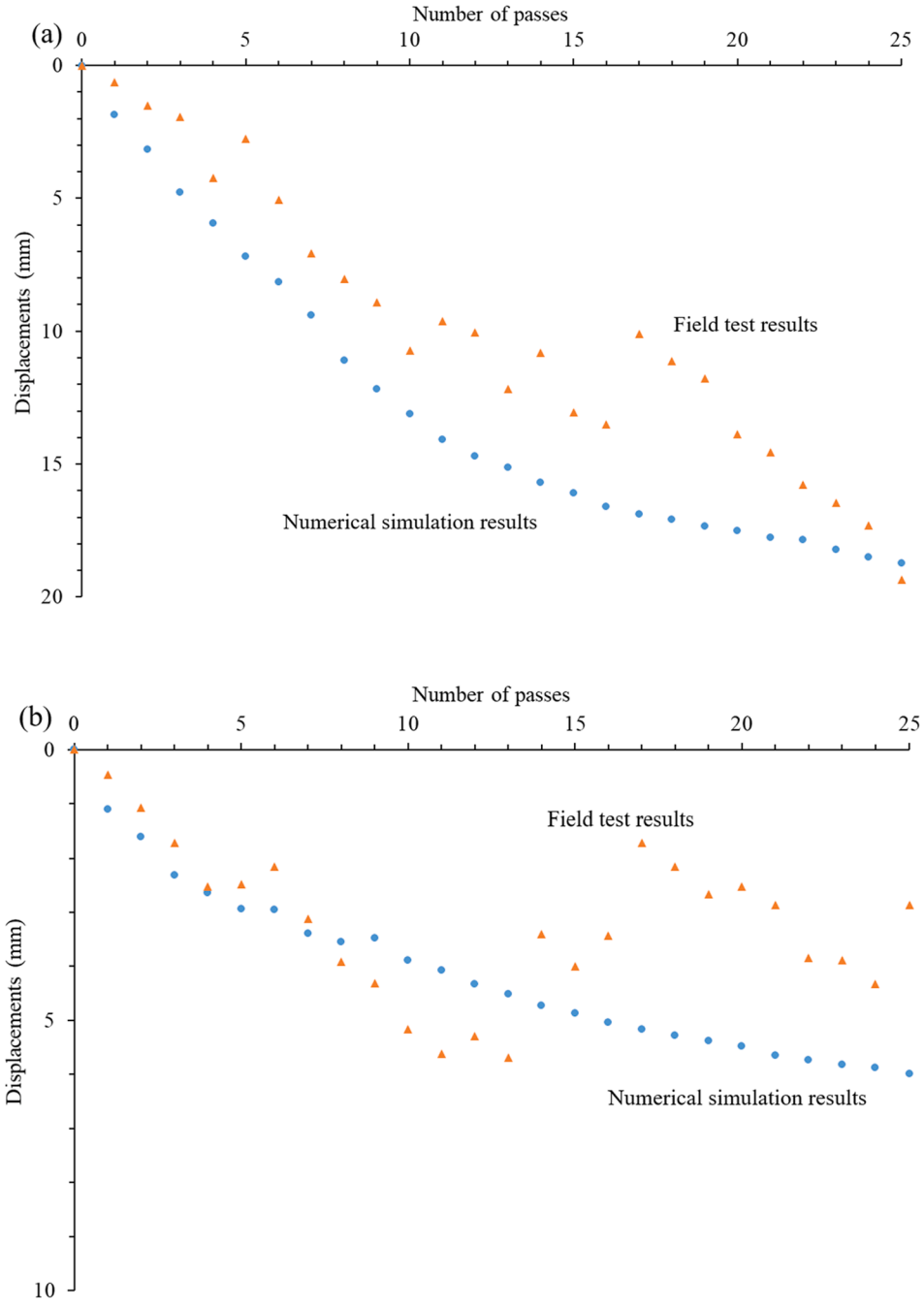

Fig. 8. Vertical displacements obtained from the numerical model and field tests, with respect to number of passes, at: (a) 0.7 m depth, (b) 1.1 m depth.

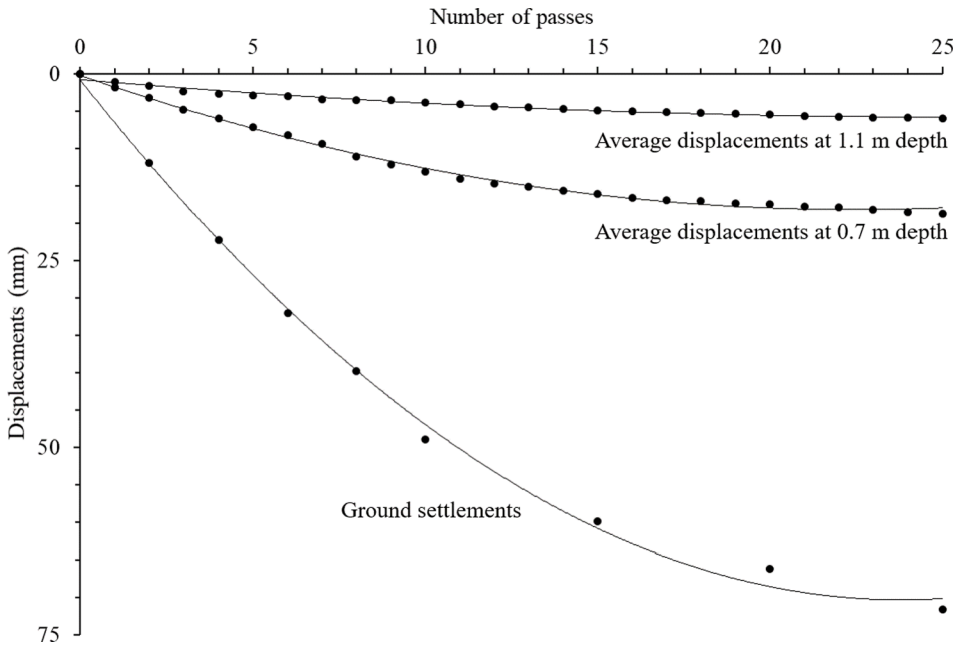

Fig. 9. Average vertical displacements at different depths with respect to number of passes from the numerical model.

4.2. Peak pressures

The peak pressure recorded at different depths below the ground surface reflects the influence of RDC within the soil body. As mentioned above, pressures induced by RDC were measured by EPCs in the field tests. The diameter of the EPCs is 230 mm, which equates to approximately 17.7 mm at the scale of the numerical model [Eq. (7)]. The D_{50} of the particles is approximately 7 mm, therefore, pressures are averaged over three adjacent particles. It is worth mentioning that, numerical pressures obtained from one particle are calculated based on the resultant force acting on that particle, and the resultant force is determined by summing the contact forces and externally applied forces acting on that particle (Davidson et al., 2015). A single particle interacts with at least 4 to 5 surrounding particles in the simulations. Therefore, the numerical pressures are calculated from the contact forces between up to 15 particles. Additionally, the pressures induced by the module are significantly affected by the offset distance (this is presented in detail below), hence, the particles used to determine the average pressures should be limited to a relatively small number to ensure accuracy at a given offset distance. This is similar to the measurement of pressures in the field tests. At each depth, the EPCs were placed at a single location over the 4 m length trial pad to measure pressures with respect to offset distance (Fig. 2). Peak pressures recorded at each module pass from numerical simulations are included in Figs. 10–12 and are upscaled using Eq. (11) in order to facilitate comparison with the field measurements. Fig. 10 shows the measured numerical and field peak pressures versus the number of passes at 0.7 and 1.1 m depths. There is no clear relationship between the peak pressures and the number of passes for both the numerical results and field data. It is evident that the value of recorded peak pressure varies for each pass. The reason for this is that the RDC module typically impacts the ground at a different location with each pass, which results in the offset distance between the centre of the module and EPC varying with each pass. The peak pressure measured for each pass from the numerical model cannot be directly compared with those recorded in field tests, since the offset distance for each pass is different in the numerical model and the field tests.

Fig. 11 presents box plots of the measured numerical and field peak pressures. The field peak pressures at 0.7 m depth have minimum and maximum pressures of 104 and 685 kPa, respectively, with a mean value of 392 kPa and standard deviation of 177 kPa. Numerical peak pressures at 0.7 m depth have minimum and maximum pressures of 235 and 858 kPa, respectively, with a mean value of 438 kPa and standard deviation of 158 kPa. Although the numerical results yield a greater maximum pressure than that measured in the field at 0.7 m depth, the results from the numerical model have a similar mean and standard deviation values as those calculated from the field tests. The numerical results at a depth of 1.1 m have mean and standard values of 366 and 107 kPa, respectively, whereas, the field measurements have a mean of 391 kPa and standard deviation of 121 kPa. The average pressure at 1.1 m depth from the numerical model is consistent with that measured in field study. It can be observed that the average pressures predicted by the numerical model are consistent with those recorded in the field trial at both 0.7 and 1.1 m depths. However, as indicated by the quartiles, the numerical peak pressures have a narrower range of variation when compared with those recorded in the field. One possible reason may be the adoption of spherical particles in the numerical model which results in a wider load distribution angle that spreads the imposed pressure over a greater area and subsequently reduces the variation in pressure. Another reason may relate to the variation in the void ratios of the soil in the field. As mentioned above, the field void ratio of the soil varies with depth, as a natural consequence of its placement, which may affect the propagation of pressure waves within the soil body and this is likely to cause greater variation in the pressure measurements.

In the numerical simulations, pressures are averaged over three particles located adjacent to each other. The coordinates of these three particles are also averaged, and the distance between the averaged coordinates and the centre of the module face, is taken as the offset distance for each module pass. The relationship between peak pressures and offset distance is presented in Fig. 12. It can be seen that recorded peak pressures have a strong relationship with the offset distance in the field tests. In addition, the variation of offset distance confirms that the RDC module impacts the ground at a different location at each pass, and it is a random process for the module to strike the ground either in front of or behind the EPCs. As can be observed, the same conclusion can be drawn from the numerical results. As shown in Fig. 12, higher pressures are imparted to the soil when the EPCs are located in front of the roller, and the distance between the EPCs and the centre of the module is between 200 and 650 mm in the numerical model and field tests at both 0.7 and 1.1 m depths. Fig. 12 also demonstrates the pressure distribution beneath the contact face between the roller module and the soil is non-

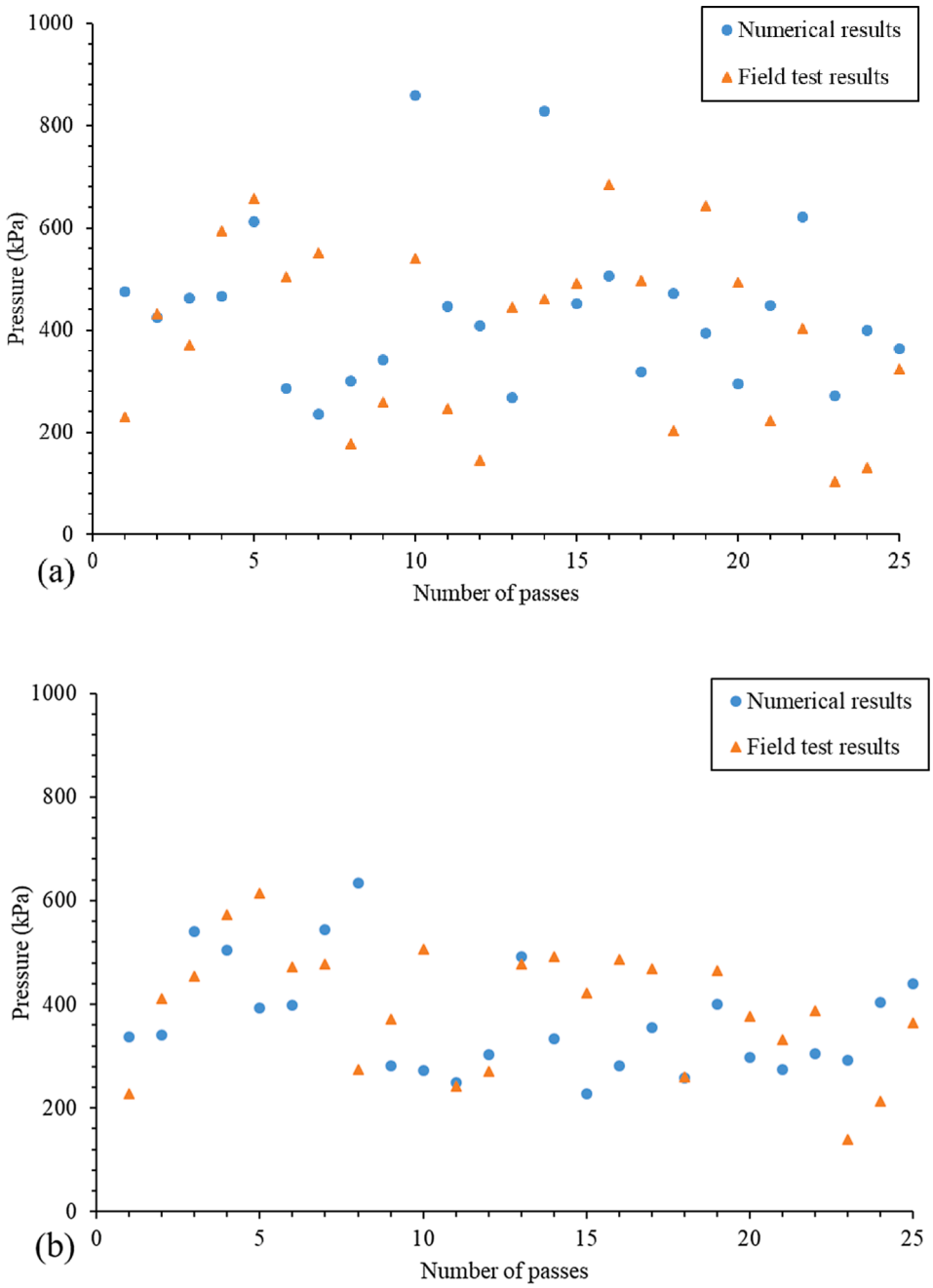

Fig. 10. Pressures obtained from the numerical and field tests, at: (a) 0.7 m depth, (b) 1.1 m depth.

uniform. As shown in Fig. 12a, numerical peak pressures with respect to the offset distance exhibit similar trends to those of the field data at 0.7 m depth. At 1.1 m depth (Fig. 12b), when compared with the field data, the numerical model yields smaller peak pressures and this may be explained by a wider load distribution angle caused by spherical particles in numerical simulations that lowers the pressures at deeper depths, as suggested earlier. Therefore, in general, it can be concluded that the numerical model provides reasonable predictions of the peak pressures imparted by the module, and the distribution of peak pressures with respect to offset distance. In addition, the plots of peak pressures against offset distance in Fig. 12 also show that the offset distance has a greater influence on peak pressures at shallow depths (0.7 m). A similar observation was reported by Scott et al. (2020), who plotted peak pressures with offset distance at 0.5, 1.0, and 1.5 m depths below the ground. They stated that the effects of offset distance on peak pressure decrease with increasing depth because the energy imparted by RDC diminishes radially from the centre of the impact with depth.

4.3. Energy imparted by RDC

Scott et al. (2019b) quantified the effects of RDC in terms of the work done on the soil from measured force–displacement data obtained from the field tests. They calculated the force–displacement data from the pressure–displacement measurements obtained from EPCs and accelerometers, and the plot of the force versus displacement was integrated to quantify the work done on the soil at a single location. If the force–displacement curves for all of the soil particles within the module influenced region are plotted, the total work done on the subsurface profile by a single module impact can be calculated, and then the total energy delivered to the ground can be quantified. However, the process of obtaining force–displacement curves for all soil particles within the module influenced region is impractical and unnecessary. In fact, the

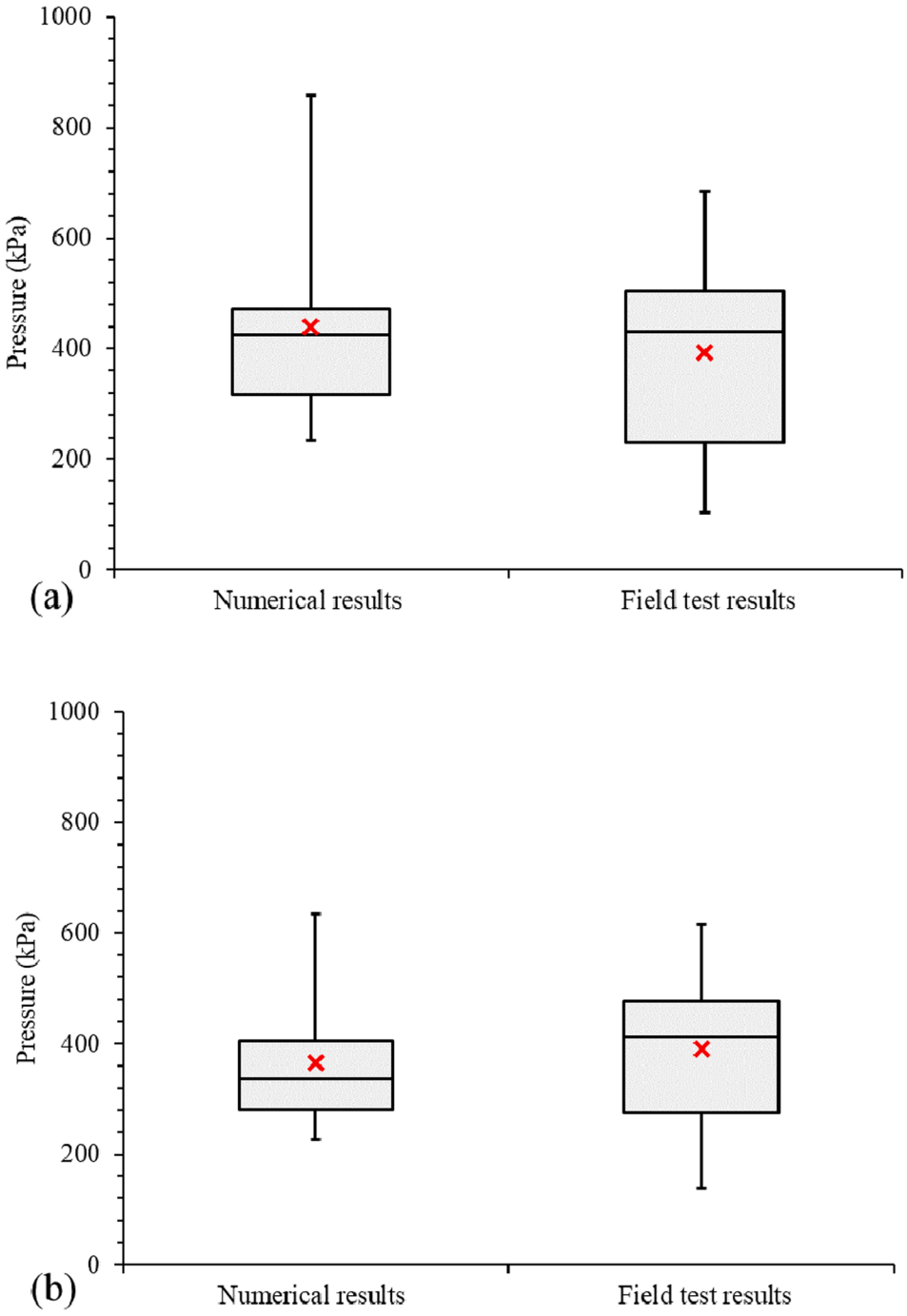

Fig. 11. Box plots of peak pressures obtained from the numerical and field tests, at: (a) 0.7 m depth, (b) 1.1 m depth.

energy imparted by the module at each impact is calculated directly by LS-DYNA, based on the motion of the roller module. As mentioned above, the motion (horizontal and rotational speeds) of the roller module is defined in the numerical RDC model according to the full-size module speed used in the field tests. The vertical speed of the roller module is calculated by the numerical model, based on the horizontal and rotational module speeds, the ground conditions and the undulating surface induced by the module. The drop height of the module at each impact is also predicted by the numerical model. The energy results from LS-DYNA are interrogated from several module impacts and then upscaled using Eq. (12). It is determined, with 95% confidence, that the module delivers approximately 24 ± 3 kJ to the ground at each impact. This value is compared with the energy equation proposed by Bradley et al. (2019) shown in Eq. (13):

$$E_{Roller} = \frac{1}{2} \times M_{Roller} \times \left(v_y^2 + v_z^2\right) + \frac{1}{2} \times I_{Roller} \times \omega_y^2 + M_{Roller} \times g \times h_{Roller} \tag{13}$$

where E_{Roller} is the energy of the roller;M_{Roller} is the mass of the roller; I_{Roller} is the mass moment of inertia of the roller; h_{Roller} is the height of the roller's centroid above the ground surface; and v_y, v_z, and ω_y are the horizontal, vertical, and angular velocities, respectively.

The energy delivered to the ground is a result of the changes in the energy of the roller during each impact. Therefore, the relationship shown in Eq. (14) can be derived from Eq. (13), and is used to calculate the energy transferred by the roller to the underlying soil.

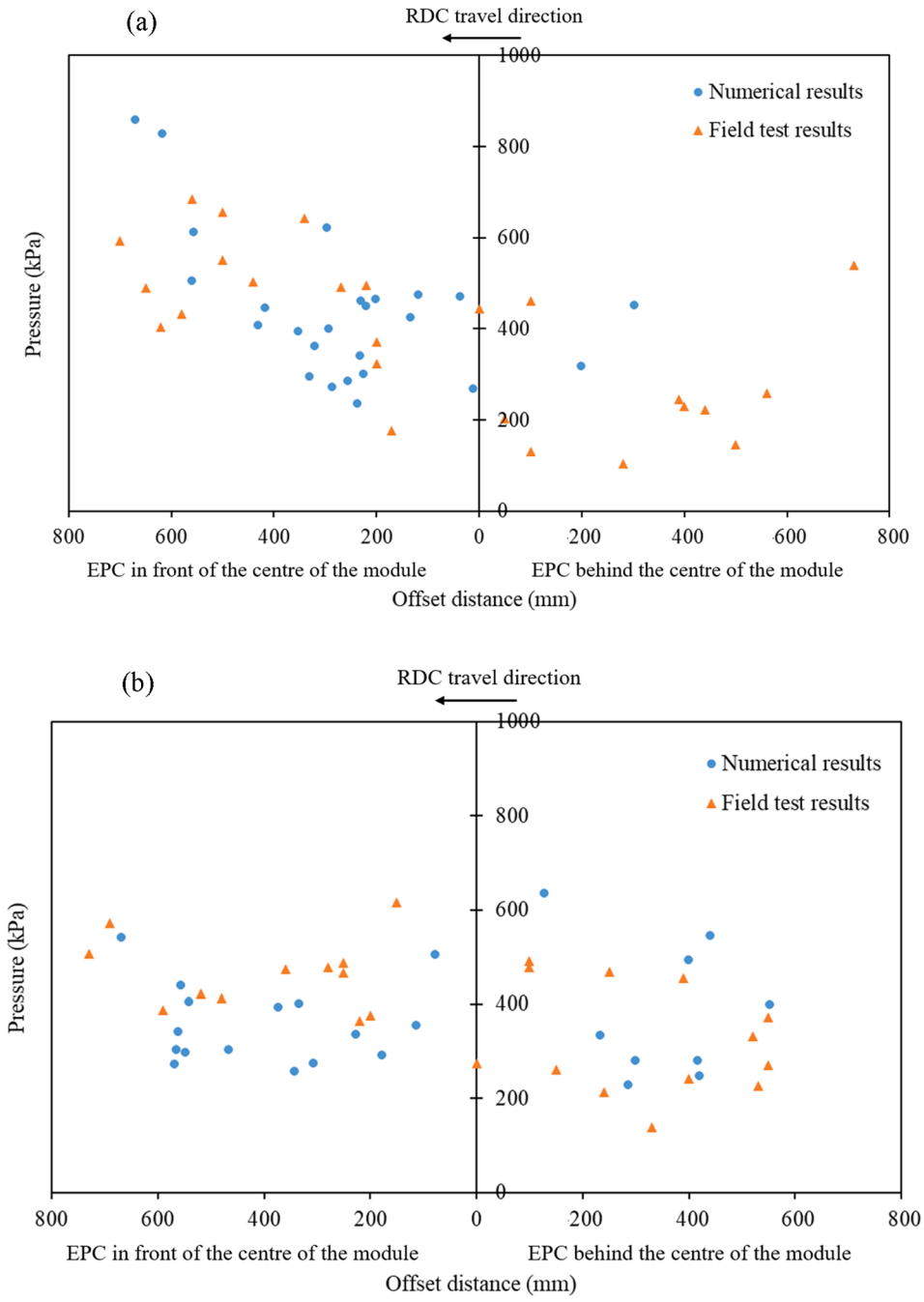

Fig. 12. Peak pressures versus offset distance obtained from the numerical and field tests, at: (a) 0.7 m depth, (b) 1.1 m depth.

$$\Delta E=\frac{1}{2}\times M_{Roller}\times\left(v_{zi}{}^{2}-v_{zf}{}^{2}\right)+\frac{1}{2}\times I_{Roller}\times\left(\omega_{yi}{}^{2}-\omega_{yf}{}^{2}\right)+M_{Roller}\times g\times\Delta h_{Roller} \quad (14)$$

where v_{zi} and v_{zf} are the vertical velocities before and after the roller impact, respectively; ω_{yi} and ω_{yf} are the angular velocities before and after the roller impact, respectively; and Δh_{Roller} is the module drop height after impact.

In the simulations, the horizontal velocity of the module is constant (235 mm/s), and the vertical velocity changes with respect to time, which results in changes in angular velocity. A random impact is selected to calculate the energy delivered to the soil using Eq. (14). The vertical velocities before and after this impact are 46.7 and –30 mm/s, respectively, where a positive vertical velocity implies that the module moves upwards and vice versa. Therefore, angular velocities before and after this module impacts the soil are 4.11 and 2.99 rad/s, respectively. Eq. (9) is then applied to upscale the velocities. The Δh_{Roller} is approximately 10.5 mm during this impact, which corresponds to 0.14 m in the full-size module. The I_{Roller} is 2.631×10^{9} kg.mm^2 for the full-size module (Bradley et al., 2019). By substituting the full-size module values of velocities, Δh_{Roller}, I_{Roller} and M_{Roller} into Eq. (14), the energy imparted by a single impact is calculated as approximately 22 kJ. Based on Eq. (13), the peak kinetic energy of the roller at impact is also calculated as approximately 61 kJ. As a result, the energy delivered to the soil at each module impact calculated from Eq. (14) is thus consistent with that obtained from LS-DYNA. In addition, Scott et al. (2020) reported the energy delivered to the ground by RDC is approximately 27 kJ for an operating speed of 11 km/h. It is important to note that the 27 kJ is the maximum theoretically possible energy imparted into the ground, and this value may not be achieved at every impact since ground

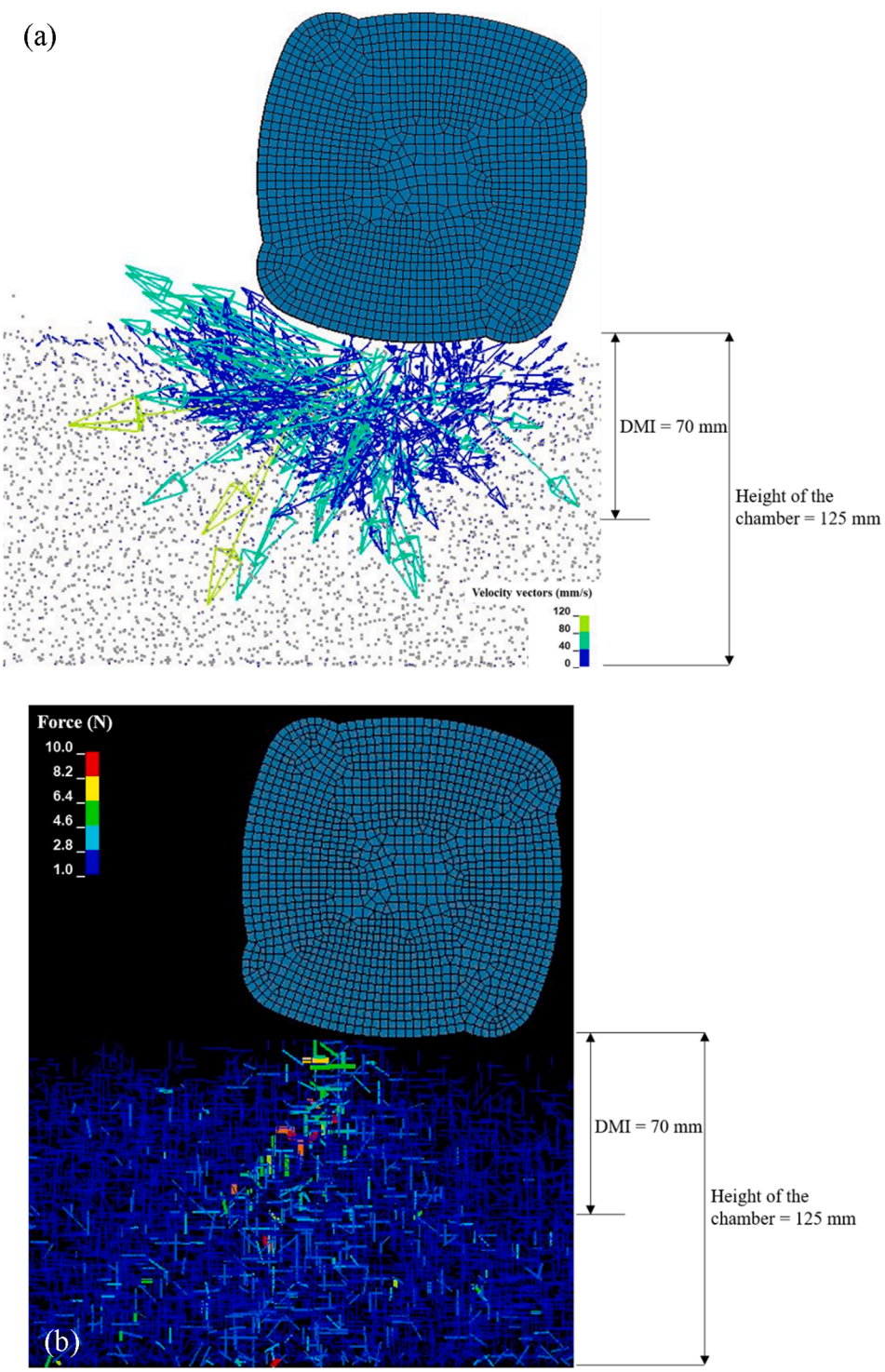

Fig. 13. Numerical results of soil particles at the 25th module pass: (a) velocity vectors, (b) force chains.

conditions affect the delivery of potential energy. The energy imparted to the soil predicted by LS-DYNA fits well with that stated by Scott et al. (2020). Therefore, it can be concluded that the LS-DYNA predicts well the RDC impact energy.

4.4. Depth of major improvement

The improvement of the underlying soil can be inferred from pressure readings, however, as the soil density increases, pressure waves are more readily able to be propagated, which results in measurable pressure readings at deeper depths. However, soil particles located at those deeper depths may not experience any permanent displacements (hence, increase in density). On the other hand, several researchers have focussed on the depth of influence, which was defined by Kim (2011) as being equivalent to the depth at which the soil has a vertical stress equal to approximately 10% of the applied stress at the ground surface. In contrast, Scott et al. (2019a) suggested that the depth of major improvement (DMI) is a more appropriate measure to determine the thickness of layers that can be compacted by RDC. DMI implies the depth of soil over which, the soil is improved to meet the target criterion that

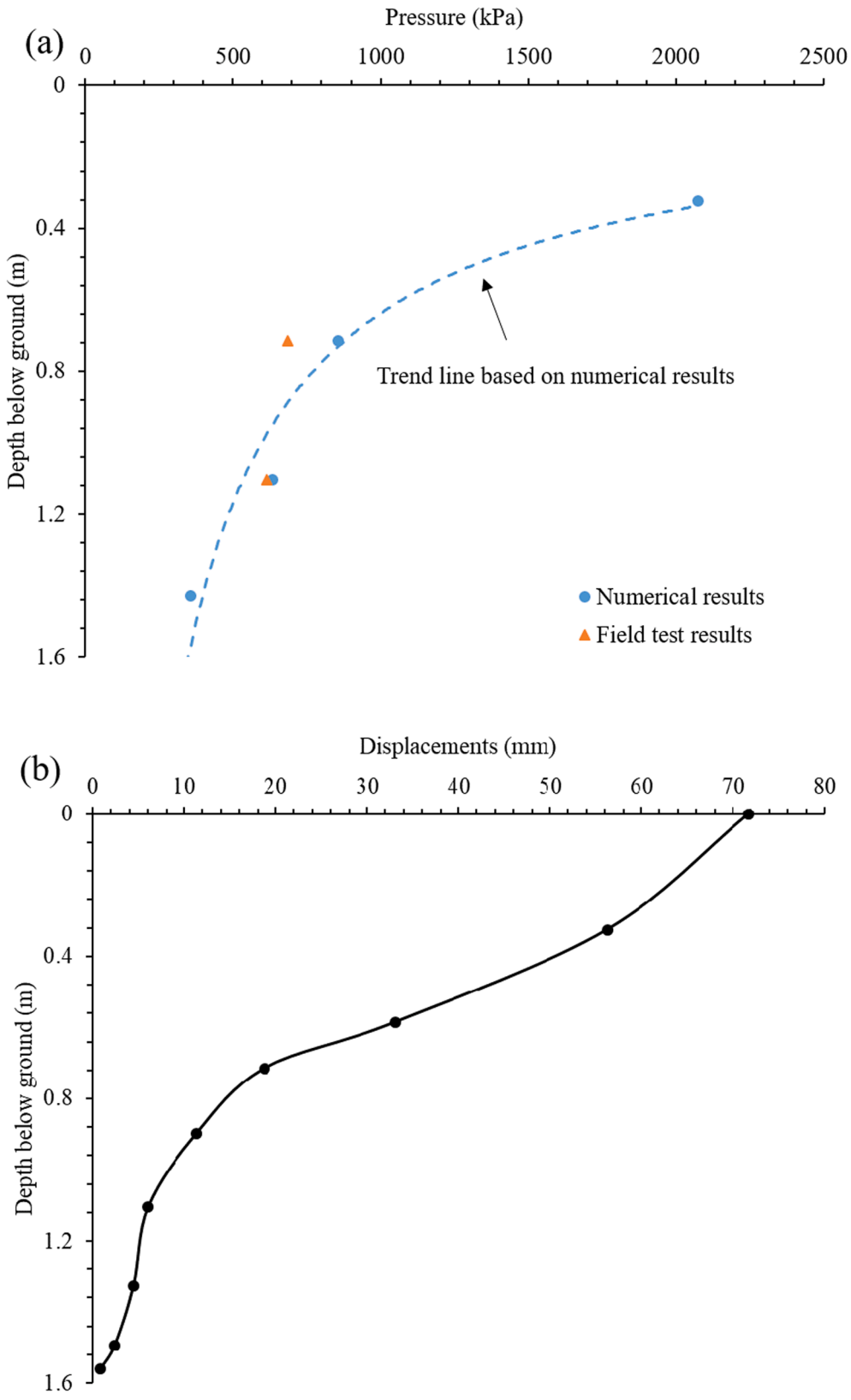

Fig. 14. Pressures and displacements at different depths: (a) peak pressures over 25 module passes, (b) soil displacements predicted by the numerical model after 25 module passes.

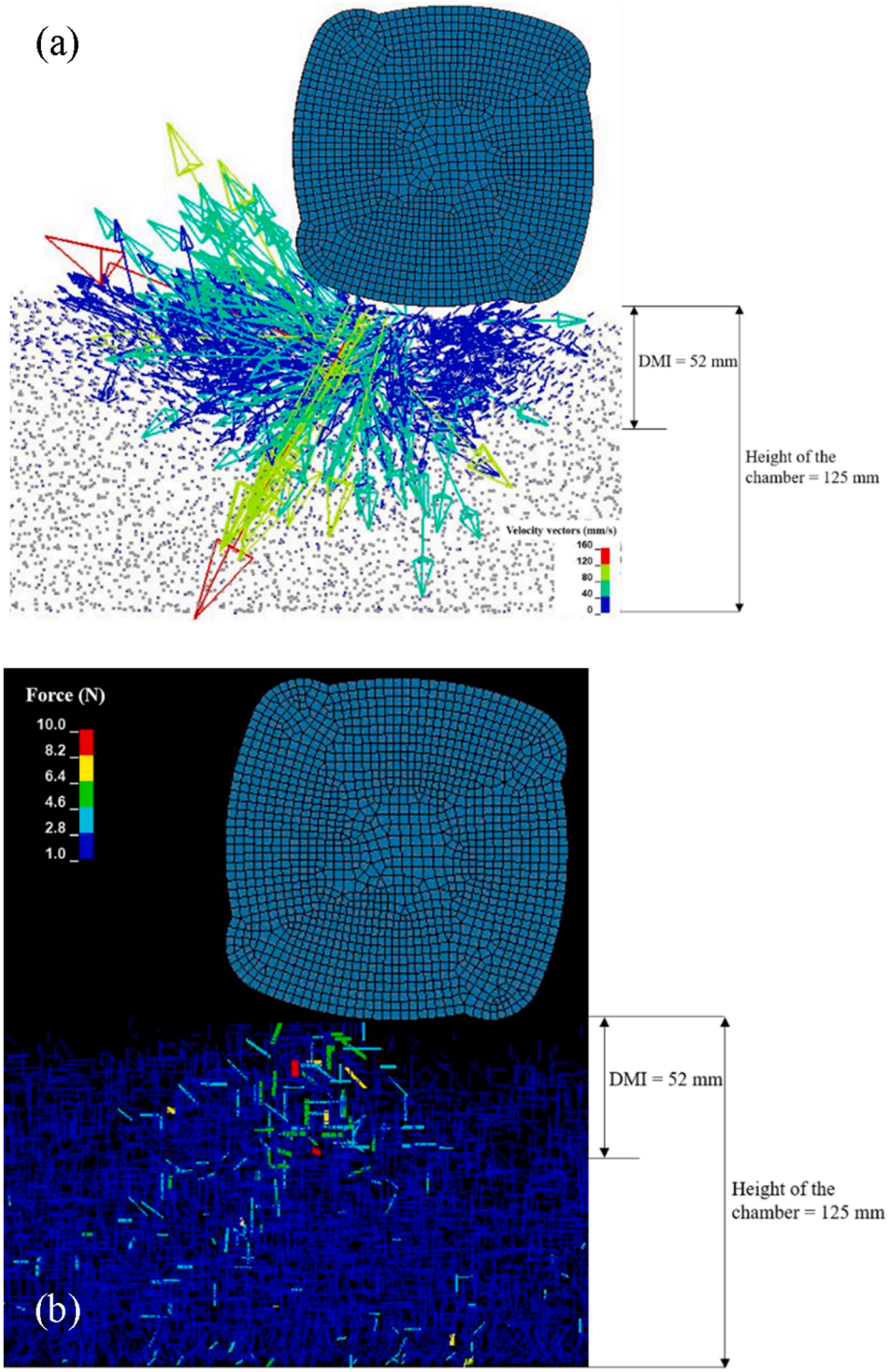

Fig. 15. Numerical results of soil particles at the 5th module pass: (a) velocity vectors, (b) force chains.

can be achieved by conventional compaction equipment in thin lifts. The relationship shown in Eq. (15) is proposed by Scott et al. (2019a) to calculate DMI.

$$\mathrm{DMI} = r \cdot k \cdot (n\sqrt{m\Delta h}) \tag{15}$$

where r is a constant (0.5–0.67); k is the ratio of the energy delivered to the ground divided by the change in gravitational potential energy at each impact; n is an empirical factor which relates to soil conditions (0.3–0.8); m is the mass of the roller module in tonnes; and Δh is module drop height after impact in metres.

The DMI in the numerical RDC model is calculated using Eq. (15). The average module drop height after impact (Δh) is approximately 11.5 mm in the numerical model, which corresponds to 0.15 m in the full-size module. Therefore, the average change in potential energy due to the lift height of the roller per module impact ($mg\Delta h$) is approximately 11.7 kJ. The k value is then obtained based on the ratio between energy imparted to the underlying soil (24 kJ demonstrated in the previous section) and the average change in potential energy (11.7 kJ), which is approximately 2.05. The value of n varies between 0.3 and 0.8.

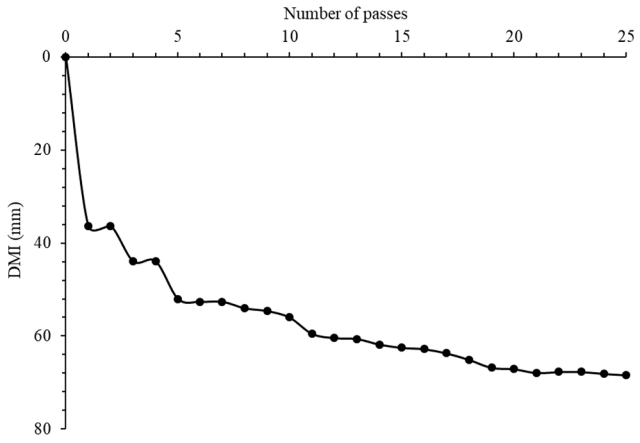

Fig. 16. DMI versus number of passes.

As proposed by Mayne et al. (1984) and Scott et al. (2019a), for granular soil, higher values of n apply. Sandy gravel soil is used in this study, therefore, $n = 0.8$ is adopted. By substituting the values of k, n, m and Δh into Eq. (15), for the full-size model, DMI = 0.9 to 1.2 m. For the 1:13 scale model (Eq. (7) is adopted to account for the 1:13 geometric ratio), DMI = 69 to 92 mm.

The calculated value of DMI proposed by Scott et al. (2019a) is compared against that obtained from the numerical model based on movement of soil particles. As stated earlier, RDC improves the density of the ground by applying mechanical energy to reduce air voids and rearrange, and in some cases fracture, the soil particles. Therefore, the movement of the underlying soil is a direct indicator of the effectiveness of RDC. Velocity vectors and force chains obtained from the numerical model at the 25th module pass are shown in Fig. 13. From Fig. 13, it is clear that there is a region where soil particles located within this zone have greater velocities (hence, displacements). The depth of this zone is approximately 70 mm, which sits within the range of DMI calculated from Eq. (15). Forces acting on soil particles are transmitted through contacts between the particles and, in order to visualize the propagation of forces, lines are used to represent contact forces between particles, which are known as force chains (LSTC, 2018). During the compaction processes, former force chains collapse and new force chains are established. According to Muthuswamy and Tordesillas (2006), a force chain is formed by a set of contacts between particles that carries the majority of the load. The main direction of the force chain is generally consistent with the orientation of the applied stress (Majmudar and Behringer, 2005). From Fig. 13b, greater contact forces can be observed within the DMI. Although there are contact forces developed below the DMI region, these low contact forces are likely not to induce any significant soil improvement.

In addition, in order to investigate the relationship between induced pressures, soil displacements and DMI, the maximum pressures measured over 25 passes, and the soil displacements recorded after 25 module passes, are plotted with respect to depth in Fig. 14. The numerical soil displacements and pressures presented in Fig. 14 were upscaled using Eqs. (10) and (11), respectively. The trend line is obtained from the numerical peak pressures, and the field peak pressures are superimposed for reference purposes. In the field tests, the pressures were measured at only two depths, hence only two field points are available. As one would expect, both pressures and soil displacements decrease with increasing depth because the compactive energy dissipates with depth. It can be seen that, the pressure and soil displacement plots follow similar trends, which suggests that soil displacements are strongly related to the induced pressures, as one would expect. The major difference between the pressure and soil displacement plots is that soil displacement is less than 5 mm after 25 passes below 1.2 m and it closes to zero near 1.5 m depth, however, the trend line of pressure suggests that pressure is still measureable below 1.5 m depth. This is consistent with the force chains plot presented earlier in Fig. 13b. As suggested previously, these low pressures at greater depths are unlike to produce any significant improvement in soil density. Additionally, pressures presented in Fig. 14a are peak pressures recorded over 25 module passes and these values cannot be achieved with each module pass. It is worth noting that soil displacements less than 5 mm result in a reduction in void ratio of only 0.005 in the field tests, which is negligible. Therefore, the majority of soil displacements occur above 1.2 m depth, which is within the range of DMI calculated from Eq. (15). Hence, it is concluded that DMI calculated from Eq. (15) is consistent with that deduced from the numerical RDC model.

5. Optimum number of passes

In the field, several in situ tests are typically undertaken such as nuclear density tests, DCP testing and CPTs, to quantify the optimum number of RDC passes. However, the application of these in situ tests are limited due to the budget and time constraints, and difficulties with the testing process (Jaksa et al., 2012). Ground settlement is commonly adopted as a key indicator of ground improvement due to RDC, since the measurement of ground settlement is efficient and cost-effective. However, Scott et al. (2016) proposed that ground settlements are an inadequate indicator of ground improvement within the soil mass. As a consequence, Scott et al. (2016) buried EPCs and accelerometers in the soil at targeted depths to quantify the level and extent of ground improvement. EPCs and accelerometers provide insights into the influence of RDC within the soil body. However, their deployment and post-processing is not straightforward. Alternatively, in the present study, the numerical model is interrogated to assess whether or not it provides any insights into the optimum number of RDC passes.

Earlier, Fig. 10 presented the numerically observed peak pressures with respect to the number of passes. Theoretically, peak pressures rise with increasing passes and soil density. However, due to variations in the offset distance, the relationship is unclear. Perhaps a more helpful indicator is the displacement at different depths with respect to number of passes, which was shown earlier in Fig. 9. As can be seen, in general, soil displacements increase with the number of passes. Displacements at 0.7 and 1.1 m depths show no obvious increase after approximately 20 passes. The ground settlement increases significantly up to the first 15 passes, and thereafter it increases modestly. Velocity vectors and force chains of soil particles at the 5th pass are displayed in Fig. 15. It can be observed that, the magnitudes of the velocity vectors are greater, and the DMI is smaller at the 5th module pass when compared against the 25th pass shown in Fig. 13. Additionally, comparing with the 5th module pass, the compactive energy induced by the module at the 25th pass is transmitted to greater depths, as evidenced by more force chains formed at deeper depths, which confirms that the pressures rise with the increasing passes and soil density. However, due to the influence of the offset distance, it is difficult to obtain this relationship from the field tests. The DMI calculated at each module pass is plotted against the number of passes in Fig. 16. As can be seen, the DMI increases with the number of passes, and the most significant increase occurs during the first 5 passes and, after approximately 20 passes, the DMI plateaus. Hence, both the DMI and settlements indicate that after 20 passes, the soil has been effectively compacted and that additional passes provide only modest improvement.

In summary, pressure results are an imperfect indicator on which to assess the optimum number of RDC passes, whereas, in contrast, both DMI and soil displacements are helpful in this regard.

6. Summary and conclusions

This paper has developed and validated a FEM-DEM numerical scale model of the 4-sided, 8-tonne, Broons BH-1300 impact roller against field tests. The numerical input parameters were calibrated against

laboratory triaxial tests performed on the same type and grading of soil that was used in field tests. In the numerical RDC simulations, the RDC module, the chamber and two timber frames were described by the FEM and the soil particles were simulated by the DEM. The numerical results were compared against the field data from four aspects, namely soil displacements at different depths, peak pressures measured at each pass, the energy delivered to the underlying soil, and the depth of major improvement. It has been demonstrated that the numerical results are in very good agreement with the field observations, which suggests that the numerical model provides reasonable predictions of ground improvement due to RDC. The results obtained from the numerical model were analysed and evaluated to obtain an efficient indicator to determine the optimum number of passes. Ground settlement was recommended, since it reflected ground improvement due to RDC and it exhibited a clear relationship with the number of passes. In addition, ground settlement can be measured in a more efficient and cost-effective manner in the field.

In general, the results of this study suggest that the FEM-DEM model provides a promising and reliable means for understanding and assessing the effectiveness of RDC. It provides several benefits over field- and laboratory-based testing but, due to its heavy reliance on supercomputing facilities will, for the time being, remain a research rather than a practical tool. In addition, conclusions drawn from this study are based on one module mass and a single operating speed. Future work will extend this model by examining the optimal operating speed and also explore the effectiveness of different RDC modules.

CRediT authorship contribution statement

Yue Chen: Conceptualization, Methodology, Software, Formal analysis, Writing - original draft. **Mark B. Jaksa:** Conceptualization, Writing - review & editing, Supervision. **Yien-Lik. Kuo:** Writing - review & editing, Formal analysis. **Brendan T. Scott:** Conceptualization, Writing - review & editing, Formal analysis.

Declaration of Competing Interest

The authors declare that they have no known competing financial interests or personal relationships that could have appeared to influence the work reported in this paper.

Acknowledgements

The authors wish to acknowledge the computational resources provided by the Phoenix HPC service at the University of Adelaide. The authors are also wish to thank the following final year undergraduate students who contributed to the test results referred to within this paper: Stefan Chenoweth, Jordan Colbert, Julianne Saw, Ross Vince, Dan Nguyen, Keegan Steele, Samuel Brown and Thomas Muecke.

References

Altaee, A., Fellenius, B.H., 1994. Physical modeling in sand. Can. Geotech. J. 31, 420–431.
Avalle, D., Carter, J., 2005. Evaluating the improvement from impact rolling on sand. Proc. 6th Int. Conf. on Ground Improvement Techniques, Coimbra, Portugal, pp. 1-8.
Avalle, D., Grounds, R., 2004. Improving pavement subgrade with the“ square” impact roller. SATC 2004.
Avalle, D.L., McKenzie, R.W., 2005. Ground improvement of landfill site using the square impact roller. Australian Geomechanics 40, 15–21.
Avsar, S., Bakker, M., Bartholomeeusen, G., van Mechelen, J., 2006. Six sigma quality improvement of compaction at the New Doha International Airport Project. Terra et aqua 103, 14.
Bouazza, A., Avalle, D.L., 2006. Effectiveness of rolling dynamic compaction on an old waste tip. In: ISSMGE 5th International Congress on Environmental Geotechnics, Cardiff, p. 1.
Bradley, A.C., Jaksa, M.B., Kuo, Y.-L., 2019. Examining the kinematics and energy of the four-sided impact roller. Proceedings of the Institution of Civil Engineers - Ground Improvement, 172, 297-304.
Calvetti, F., Viggiani, G., Tamagnini, C., 2003. A numerical investigation of the incremental behavior of granular soils. Rivista italiana di geotecnica 37, 11–29.
Chen, Y., Deng, A., Wang, A., Sun, H., 2018. Performance of screw–shaft pile in sand: Model test and DEM simulation. Comput. Geotech. 104, 118–130.
Chen, Y., Jaksa, M., Kuo, Y., Airey, D., 2021. Experimental analysis of rolling dynamic compaction using transparent soils and particle image velocimetry. Can. Geotech. J. https://doi.org/10.1139/cgj-2020-0573.
Chou, H., Lee, C., Chung, Y., Hsiau, S., 2012. Discrete element modelling and experimental validation for the falling process of dry granular steps. Powder Technol. 231, 122–134.
Chung, O., Scott, B., Jaksa, M., Kuo, Y., Airey, D., 2017. Physical modeling of rolling dynamic compaction. Proceedings of the 19th Int. Conf. on Soil Mechanics and Geotechnical Engineering, Seoul, Korea, Sept. 18–22, 905–908.
Ciantia, M., Arroyo Alvarez De Toledo, M., Calvetti, F., Gens Solé, A., 2015. An approach to enhance efficiency of DEM modelling of soils with crushable grains. Géotechnique, 65, 91-110.
Ciantia, M.O., Arroyo, M., Butlanska, J., Gens, A., 2016. DEM modelling of cone penetration tests in a double-porosity crushable granular material. Comput. Geotech. 73, 109–127.
Coetzee, C., 2016. Calibration of the discrete element method and the effect of particle shape. Powder Technology, 297, 50-70.
Coetzee, C.J., 2017. Review: Calibration of the discrete element method. Powder Technology, 310, 104-142.
Cundall, P.A., Strack, O.D., 1979. A discrete numerical model for granular assemblies. Geotechnique 29, 47–65.
Davidson, M.T., Chung, J.H., Teng, H., Han, Z., Le, V., 2015. Volume-Averaged Stress States for Idealized Granular Materials using Unbonded Discrete Spheres in LS-DYNA®. 10th European LS-DYNA Conference, Würzburg, Germany.
de Bono, J., McDowell, G., Wanatowski, D., 2015. Investigating the micro mechanics of cemented sand using DEM. Int. J. Numer. Anal. Meth. Geomech. 39, 655–675.
Evans, T.M., Valdes, J.R., 2011. The microstructure of particulate mixtures in one-dimensional compression: numerical studies. Granular Matter 13, 657–669.
Feng, Y., Owen, D., 2014. Discrete element modelling of large scale particle systems—I: exact scaling laws. Comput. Particle Mech. 1, 159–168.
Forsström, D., Jonsén, P., 2016. Calibration and validation of a large scale abrasive wear model by coupling DEM-FEM: Local failure prediction from abrasive wear of tipper bodies during unloading of granular material. Eng. Fail. Anal. 66, 274–283.
Gabrieli, F., Cola, S., Calvetti, F., 2009. Use of an up-scaled DEM model for analysing the behaviour of a shallow foundation on a model slope. Geomech. Geoeng.: Int. J. 4, 109–122.
González-Montellano, C., Fuentes, J., Ayuga-Téllez, E., Ayuga, F., 2012. Determination of the mechanical properties of maize grains and olives required for use in DEM simulations. J. Food Eng. 111, 553–562.
Jaksa, M.B., Scott, B.T., Mentha, N., Symons, A., Pointon, S., Wrightson, P., Syamsuddin, E., 2012. Quantifying the zone of influence of the impact roller. ISSMGE-TC 211 International Symposium on Ground Improvement IS-GI Brussels, 30 May – 1 June, Vol. 2, pp. 41–52.
Jiang, M., Dai, Y., Cui, L., Shen, Z., Wang, X., 2014. Investigating mechanism of inclined CPT in granular ground using DEM. Granular Matter 16, 785–796.
Jing, X.Y., Zhou, W.H., Zhu, H.X., Yin, Z.Y., Li, Y., 2018. Analysis of soil-structural interface behavior using three-dimensional DEM simulations. Int. J. Numer. Anal. Meth. Geomech. 42, 339–357.
Kim, K., 2011. Numerical simulation of impact rollers for estimating the influence depth of soil compaction. Texas A & M University.
Kuo, Y., Jaksa, M., Scott, B., Bradley, A., Power, C., Crisp, A., Jiang, J., 2013. Assessing the effectiveness of rolling dynamic compaction. In: Proceedings of the 18th International Conference on Soil Mechanics and Geotechnical Engineering, Paris, pp. 1309–1312.
Lei, Z., Zang, M., 2010. An approach to combining 3D discrete and finite element methods based on penalty function method. Comput. Mech. 46, 609–619.
LSTC. 2018. LS-DYNA KEYWORD USER’S MANUAL. Livermore, California: Livermore Software Technology Corporation, ISBN: 0-9778540-2-7.
Majmudar, T.S., Behringer, R.P., 2005. Contact force measurements and stress-induced anisotropy in granular materials. Nature 435, 1079–1082.
Mayne, P.W., Jones Jr, J.S., Dumas, J C., 1984. Ground response to dynamic compaction. J. Geotech. Eng., 110, 757-774.
Muthuswamy, M., Tordesillas, A., 2006. How do interparticle contact friction, packing density and degree of polydispersity affect force propagation in particulate assemblies? J. Stat. Mech: Theory Exp. 2006, P09003.
Nakashima, H., Oida, A., 2004. Algorithm and implementation of soil–tire contact analysis code based on dynamic FE–DE method. J. Terramech. 41, 127–137.
Ranjan, G., Rao, A., 2007. Basic and applied soil mechanics. New Age International.
Scott, B., Jaksa, M., 2014. Evaluating rolling dynamic compaction of fill using CPT. In: Proceedings of the 3rd International Symposium on Cone Penetration Testing, pp. 941–948.
Scott, B., Jaksa, M., Mitchell, P., 2019a. Depth of influence of rolling dynamic compaction. In: Proceedings of the Institution of Civil Engineers-Ground Improvement, pp. 1–10.
Scott, B., Jaksa, M., Mitchell, P., 2019b. Ground response to rolling dynamic compaction. Géotech. Lett. 9, 99–105.
Scott, B., Jaksa, M., Syamsuddin, E., 2016. Verification of an impact rolling compaction trial using various in situ testing methods. Proc. of 5th Int. Conf. on Geotechnical and Geophysical Site Characterisation.
Scott, B.T., Jaksa, M.B., Mitchell, P.W., 2020. Influence of towing speed on effectiveness of rolling dynamic compaction. J. Rock Mech. Geotech. Eng. 12, 126–134.

Thakur, M.M., Penumadu, D., 2020. Triaxial compression in sands using FDEM and micro-X-ray computed tomography. Comput. Geotech. 124, 103638.
Xu, W., Zeng, H., Yang, P., Zang, M., 2020. Numerical analysis on tractive performance of off-road tire on gravel road using a calibrated finite element method–discrete element method model and experimental validation. Proc. Inst. Mech. Eng., Part D: J. Automobile Eng. 234, 3440–3457.
Yang, P., Zang, M., Zeng, H., 2019. DEM–FEM simulation of tire–sand interaction based on improved contact model. Comput. Particle Mech. 1–15.
Zeng, H., Xu, W., Zang, M., Yang, P., 2020. Calibration of DEM-FEM model parameters for traction performance analysis of an off-road tire on gravel terrain. Powder Technol. 362, 350–361.
Zhang, N., Arroyo, M., Ciantia, M.O., Gens, A., Butlanska, J., 2019. Standard penetration testing in a virtual calibration chamber. Comput. Geotech. 111, 277–289.
Zhou, Q., Xu, W.-J., Lubbe, R., 2021. Multi-scale mechanics of sand based on FEM-DEM coupling method. Powder Technol. 380, 394–407.